

Native qudit entanglement in a trapped ion quantum processor

Received: 18 January 2023

Accepted: 15 March 2023

Published online: 19 April 2023

 Check for updates

Pavel Hrmo ^{1,6} ✉, Benjamin Wilhelm ^{1,6}, Lukas Gerster¹, Martin W. van Mourik¹, Marcus Huber ^{2,3}, Rainer Blatt^{1,4,5}, Philipp Schindler ¹, Thomas Monz ^{1,5} & Martin Ringbauer¹

Quantum information carriers, just like most physical systems, naturally occupy high-dimensional Hilbert spaces. Instead of restricting them to a two-level subspace, these high-dimensional (qudit) quantum systems are emerging as a powerful resource for the next generation of quantum processors. Yet harnessing the potential of these systems requires efficient ways of generating the desired interaction between them. Here, we experimentally demonstrate an implementation of a native two-qudit entangling gate up to dimension 5 in a trapped-ion system. This is achieved by generalizing a recently proposed light-shift gate mechanism to generate genuine qudit entanglement in a single application of the gate. The gate seamlessly adapts to the local dimension of the system with a calibration overhead that is independent of the dimension.

Quantum computing has taken great strides in the past decades with multiple platforms demonstrating control over tens of qubits^{1–4}. However, scaling these systems to a regime beyond the capabilities of classical computers remains very challenging, both in terms of increasing the size of the quantum computational Hilbert space, and in terms of increasing the depth of the computational circuits. A significant potential for tempering these daunting scaling demands, however, lies in plain sight when appreciating that the quantum systems we use are multi-level, not two-level systems. A natural way to extend the computational Hilbert space and reduce circuit complexity, without increasing the complexity of quantum devices is thus to use the full multi-level or qudit structure of existing quantum information carriers such as trapped ions, see Fig. 1.

Qudit control has already been demonstrated in a number of architectures^{5–16}, including trapped ions^{17–20}. Qudit approaches not only enable reduced circuit complexity²¹ and simplifications of virtually any quantum circuit²², but also benefit from more powerful quantum error correction^{23–26}, and enable the implementation of optimal quantum measurements²⁷ as well as native quantum simulation of a range of physical systems such as lattice gauge models^{28,29},

optimization problems³⁰, or quantum chemistry³¹. The key to these advantages, however, is an appropriate set of quantum operations. While for qubits all entangling gates are equal up to local rotations, the same is not true for qudits, where the richer Hilbert space allows for different forms of coherence⁶ and entanglement³². We can roughly classify qudit entangling gates by their entangling power, i.e., the amount of entanglement that is created relative to a maximally entangled state of two qubits. While in principle already the simplest gate, a qubit entangling gate embedded in a higher-dimensional Hilbert space, would suffice for universal qudit quantum computation^{17,33}, having access to a range of gates with different entangling power will be crucial for unlocking the full potential of a qudit quantum processor. Not only will a diverse set of interactions enable the direct simulation of a wider range of physical systems, but it will also enable much more efficient quantum circuit decomposition.

Here we describe and demonstrate a native qudit entangling gate in a trapped-ion quantum processor. Being based on differential light shifts between the ground- and excited state manifolds on an optical transition, the gate action can be made symmetric on all excited qudit states. We show that this implies that the same gate mechanism can be

¹Institut für Experimentalphysik, Universität Innsbruck, Technikerstraße 25/4, 6020 Innsbruck, Austria. ²Atominstytut, Technische Universität Wien, 1020 Vienna, Austria. ³Institute for Quantum Optics and Quantum Information-IQOQI Vienna, Austrian Academy of Sciences, Boltzmanngasse 3, 1090 Vienna, Austria. ⁴Institut für Quantenoptik und Quanteninformation, Österreichische Akademie der Wissenschaften, Technikerstraße 21a, 6020 Innsbruck, Austria. ⁵AQT, Technikerstraße 17, 6020 Innsbruck, Austria. ⁶These authors contributed equally: Pavel Hrmo, Benjamin Wilhelm.

✉ e-mail: pahrmo@phys.ethz.ch

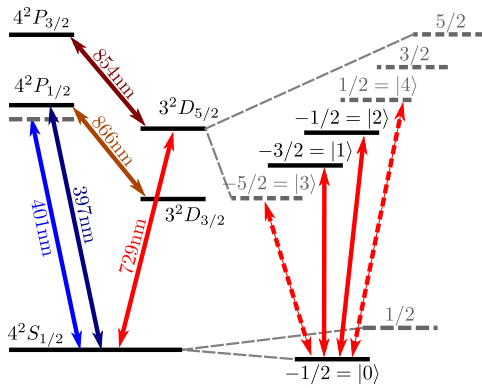


Fig. 1 | Level scheme of the $^{40}\text{Ca}^+$ ion. Encoding quantum information in the sub-levels of the $S_{1/2}$ and $D_{5/2}$ manifold allows us to increase the size of the computational Hilbert space. Coherent operations between the sub-levels can be performed using 729 nm laser light, while 401 nm light is used to generate the light shift for the state-dependent force.

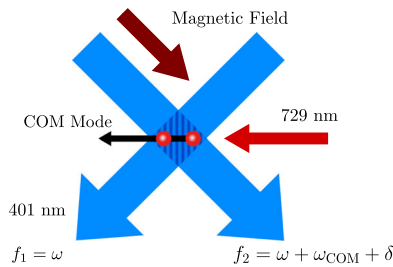


Fig. 2 | Experimental setup. Two beams with $\lambda = 401$ nm and frequencies f_1, f_2 with a relative detuning of $\omega_{\text{COM}} + \delta$ are intersected at a 90° angle to drive the state-dependent force. A 729 nm laser along the axial trap direction is used to implement local operations.

used irrespective of the qudit dimension to generate genuine qudit entanglement in the sense that the Schmidt number of the resulting state equals the qudit dimension. Crucially, this means that the experimental calibration overhead does not increase with qudit dimension. We further show that direct application of the gate can generate maximal qudit entanglement up to dimension 4. We characterize the gate dynamics and noise sources in detail, demonstrating that this gate can be a stepping stone into the world of native qudit quantum information processing with trapped ions.

Results

The principle behind the qudit entanglement generation is the application of light-shift (LS) gates, in which a state-dependent optical-dipole force couples the ions' electronic states to their common motion in the trap. Light-shift gates have been well studied for entangling hyperfine and Zeeman qubits with a pair of intersecting laser beams (see Fig. 2) that create a traveling wave^{34–37}. The traveling wave produces a spatially modulated light shift that drives an excursion in the phase space of one of the motional modes. The ions acquire a different geometric phase depending on their electronic state, leaving them in an entangled state after completing the excursion. The beams also introduce additional, unwanted local phases as the electronic states experience different light shifts. For hyperfine or Zeeman qubits, the polarization of the optical beams can be used to null these differential light shifts on the electronic states. In practice, however, these gates are typically applied with a spin echo pulse, inserted between two halves of the LS gate pulse during which the ions complete a single loop in motional phase space. This ensures that any residual light shifts between the two electronic states due to

experimental imperfections are canceled. Adding these local π pulses has the further advantage of suppressing slow qubit frequency drifts and decoupling from the optical phase of the LS gate laser. Using this technique, the LS gate can also be implemented without the requirement to intrinsically null the differential light shift. This opens the opportunity to apply the gate to qubits with an energy difference in the optical domain, without careful selection of the laser frequency. Such gates were theoretically described³⁸ and implemented³⁹ for an optical qubit formed by sub-levels of the $S_{1/2}$ and $D_{5/2}$ manifold in $^{40}\text{Ca}^+$ ions. We now describe how this gate scheme can be generalized to generate genuine qudit entanglement for qudits of arbitrary dimension encoded in the Zeeman sub-levels of the $S_{1/2}$ and $D_{5/2}$ manifolds of $^{40}\text{Ca}^+$ ions, see Fig. 1. Formally, the two-ion LS Hamiltonian, after adiabatic elimination of the excited states and application of the Lamb-Dicke and rotating-wave approximations, can be written in the interaction frame of the ions' center-of-mass (COM) motion as

$$H_{\text{LS}} = \frac{i\hbar\eta}{2} \sum_j \sum_N \Delta_{Nj} |j_N\rangle \langle j_N| e^{-i\delta t} e^{i\varphi_N} a^\dagger + \text{h.c.} \quad (1)$$

Here, Δ_{Nj} represents the light shift on the state $|j\rangle$ of ion N , δ the detuning from the motional mode frequency, η the Lamb-Dicke parameter, a^\dagger the creation operator of the motional mode and φ_N the phase determined by the inter-ion distance within the traveling wave of the laser. Integrating Eq. (1), we obtain the propagator $U_{\text{LS}}(t)$ describing a state-dependent force on the ions' motion that can be visualized as loops in motional phase space, which will periodically return to the origin after a time $t_g = 2\pi/\delta$. During the evolution in phase space, each initial electronic state combination $|jk\rangle$ of the two ions will, in the most general case, pick up a different geometric phase ϕ_{jk} after a single LS gate pulse application.

Similar to the qubit case, we can now symmetrize the geometric phases for qudits, while canceling differential light shifts. We achieve this by encoding our qudits in the $|0\rangle = S_{1/2, m_j = -1/2}$ ground state and the Zeeman sub-levels of the $D_{5/2}$ manifold as $|i\rangle$, with $i \in \{1, 2, 3, 4\}$, see Fig. 1. We then choose a wavelength close to the $S_{1/2} \leftrightarrow P_{1/2}$ transition, which for our choice of encoding results in $\Delta_{N,0} \gg \Delta_{Nj}$ for $j \neq 0$. This allows us to neglect differences in phase shifts between $D_{5/2}$ levels induced by the LS gate pulse. We interleave d applications of $U_{\text{LS}}(t_g)$ with two-ion cyclic permutations of the form $X_d = (\sum_{j=0}^{d-1} |j+1 \pmod{d}\rangle \langle j|)^{\otimes 2}$, where the populations of each level are transferred to the level with the next higher index. This ensures that each logical state spends an equal amount of time in each physical energy level. After application of the sequence $G = (X_d U_{\text{LS}}(t_g))^d$ we find the phases $\tilde{\phi}_{jk}$ imprinted on the states $|jk\rangle$

$$\tilde{\phi}_{jk} = \begin{cases} \sum_{k=0}^{d-1} \phi_{kk} & \text{if } k=j \\ \sum_{k=0}^{d-1} \sum_{j < k} \phi_{jk} & \text{else,} \end{cases} \quad (2)$$

where ϕ_{jk} refer to the phases from the constituent $U_{\text{LS}}(t_g)$ pulses. For $d=2$ the sequence $(X_2 U_{\text{LS}}(t_g))^2$ corresponds to the standard qubit light-shift gate with spin echo³⁹. Equation (2) shows that after symmetrization we are left with only two different phases, one for the cases where both ions are in the same state and one where the ions are in different states, see Fig. 3. Hence, up to a global phase, the qudit light-shift gate operation $G(\theta)$ can be described for all d by

$$G(\theta) : \begin{cases} |ij\rangle \rightarrow |ij\rangle \\ |jk\rangle \rightarrow \exp(i\theta) |jk\rangle \end{cases} \quad \text{if } j \neq k. \quad (3)$$

The operator $G(\theta)$ directly generates genuine qudit entanglement as opposed to merely embedding qubit-level entanglement in a larger Hilbert space¹⁷. This will enable the generation of high-fidelity qudit entanglement with a single gate operation. In the experiment θ can be chosen freely by simultaneously varying the gate detuning δ and the

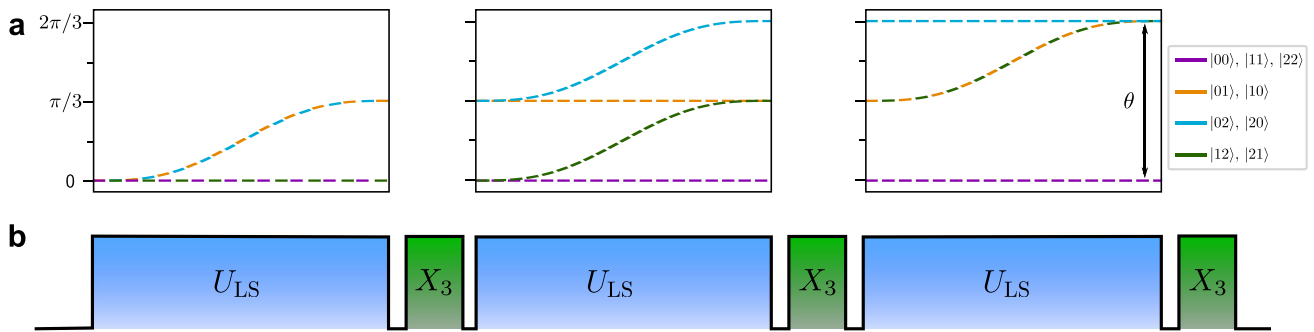


Fig. 3 | Application of the gate on two qutrits. **a** Phase evolution of the two-qutrit state components relative to the $|00\rangle$ ground state during the application of the LS gate pulses. States $|01\rangle$ and $|10\rangle$ are shown in orange, $|02\rangle$ and $|20\rangle$ in blue, and $|12\rangle$ and $|21\rangle$ in green. The equal electronic states $|00\rangle, |11\rangle, |22\rangle$ in purple do not acquire

any relative phases. **b** Corresponding pulse scheme to implement the composite qudit light-shift gate operator $G(\theta)$ for a qutrit ($d = 3$). Light-shift gate pulses $U_{LS}(t_g)$ are interlaced with cyclic permutation gates X_3 .

gate time t_g or changing the laser power in order to adjust the light shifts $\Delta_{N,j}$. A more detailed derivation of Eq. (3) for the case of a qubit and qutrit is found in the supplementary note 1.

The gate is performed on two $^{40}\text{Ca}^+$ ions, trapped 110 μm above the surface of a segmented surface Paul trap. The ion trap is mounted inside a liquid Helium flow-cryostat and is operated at $\sim 35\text{ K}^{40}$. Static potentials applied to a set of DC electrodes confine the ions along the axial direction with an axial COM mode frequency of $\omega_{\text{COM}}/2\pi \approx 1.1\text{ MHz}$. Radio-frequency potentials create radial confinement with frequencies $\{\omega_x, \omega_y\}/2\pi \approx \{3.5\text{ MHz}, 3.2\text{ MHz}\}$. Outside the vacuum chamber, a pair of Helmholtz coils aligned 45° with respect to the axial trap direction generates a magnetic field of $\sim 3.6\text{ G}$, defining the quantization axis. The $S_{1/2, m_j = -1/2}$ ground state and the sub-levels of the $D_{5/2}$ manifold are used for encoding the qudits, see Fig. 1. Single-qudit rotations between $|0\rangle$ and $|i\rangle$ are implemented using a 729 nm laser with a linewidth of $\sim 10\text{ Hz}$.

The interaction of Eq. (1) is generated by a pair of perpendicular laser beams, one of which is parallel and the other perpendicular to the applied magnetic field, each with a waist of approximately $45\ \mu\text{m}$, see Fig. 2. In this configuration, the difference wavevector of the two beams is parallel to the axial trap direction to only couple to the ions' axial motion. The two beams are derived from a single frequency-doubled Titanium-Sapphire laser at a wavelength of $\lambda \approx 401.2\text{ nm}$, approximately 8.1 THz red-detuned from the $S_{1/2} \leftrightarrow P_{1/2}$ transition. This results in low scattering errors on the order of 10^{-4} for an LS gate pulse with a duration of $t_g \sim 35\ \mu\text{s}$. The LS force on the state $|0\rangle$ is maximized by choosing both beams to be vertically polarized. The detuning between the beams is chosen as $(\omega_{\text{COM}} + \delta)$ to couple primarily to the axial COM motion.

Maximizing the differential light shift for a given beam intensity requires the inter-ion distance to be an integer or half-integer multiple of the period of the traveling wave pattern created by the LS gate beams³⁶. Imperfect spacing decreases the phase difference between equal and unequal states during the application of U_{LS} on the two ions, thus reducing the achievable gate speed for a given beam intensity. Since most error sources scale with the gate duration, correctly choosing the spacing is crucial for achieving low error rates. Experimentally, we adjust the inter-ion spacing by varying the voltages on the trap electrodes, which create the confinement in the axial direction.

The ion spacing is calibrated by initializing the ions in $|00\rangle$ and applying a resonant ($\delta = 0$) LS gate pulse with variable time. If the spacing is set to a half-integer multiple of the standing wave, the breathing mode is excited to a coherent state, whereas the motion of the COM mode remains unaffected. For an integer spacing the relation between the motional modes is inverted. The motional state is read out by measuring the excitation when shelving the ions on the respective red sideband of the $S_{1/2} \leftrightarrow D_{5/2}$ transition. By observing excitation of

only the breathing mode, we infer that the inter-ion distance is set appropriately, and the unwanted phase accumulation of the equal states is minimized.

After Doppler cooling, the ions' axial motional modes are cooled to around 0.1 quanta by resolved sideband cooling. We then initialize the ions in the $|00\rangle$ state via optical pumping. We create an equal superposition of all qudit states by applying the operator

$$P = \prod_{j=1}^{d-1} R^{0j}(\vartheta_j, 0), \quad (4)$$

with rotation angle $\vartheta_j = 2 \arcsin(1/\sqrt{j+1})$ and

$$R^{j,k}(\vartheta, \phi) = \exp\left(-i \frac{\vartheta}{2} (\sigma_1^{j,k}(\phi) + \sigma_2^{j,k}(\phi))\right) \quad (5)$$

where $\sigma_N^{j,k}(\phi) = \cos(\phi)\sigma_x^{j,k} + \sin(\phi)\sigma_y^{j,k}$ denotes the rotation on ion N on the transition $|j\rangle \leftrightarrow |k\rangle$ for Pauli matrices σ_x, σ_y . Each rotation $R^{j,k}(\vartheta, \phi)$ is implemented by a resonant 729 nm laser pulse, where ϕ is determined by the laser phase and ϑ by the pulse area. We then apply the sequence $(X_d U_{LS}(t_g))^d$, where the generalized spin echo X_d is implemented by a sequence of π -pulses on the $|0\rangle \leftrightarrow |j\rangle$ transitions. For $d > 2$ the phase of the first laser pulse of each X_d is shifted by π to decrease the errors due to over-rotation of the local pulses, leading to a sequence of

$$X_d = \prod_{j=1}^{d-1} R^{0j}(\pi, \delta_{j1} \pi) \quad (6)$$

for the permutation operator, where δ_{ij} denotes the Kronecker delta. After the final permutation, we apply the conjugate P^\dagger of the initial preparation sequence. Up to dimension $d = 4$, this leaves the system in a maximally entangled state of the form $|\Psi_d\rangle = \sum_j^{d-1} |jj\rangle / \sqrt{d}$, whereas for $d = 5$ the sequence will result in the state $|\Psi_5\rangle = (3|00\rangle + 2\sum_{j=1}^4 |jj\rangle) / 5$. This is likely a consequence of there only being a single phase applied to all $d^2 - d$ components of the state. In order to generate maximal entanglement in higher dimensions it might thus be necessary to use multiple applications of the gate, or generalize the gate action such that it imparts different phase shifts to different state components.

We can directly estimate the state fidelity and the amount of entanglement of the generated states from the relative amplitudes of the components $|ii\rangle$, as well as their pairwise coherences. Experimentally, the population of the $|00\rangle$ state can be measured by driving the $S_{1/2} \leftrightarrow P_{1/2}$ transition with a 397 nm laser and collecting the fluorescence

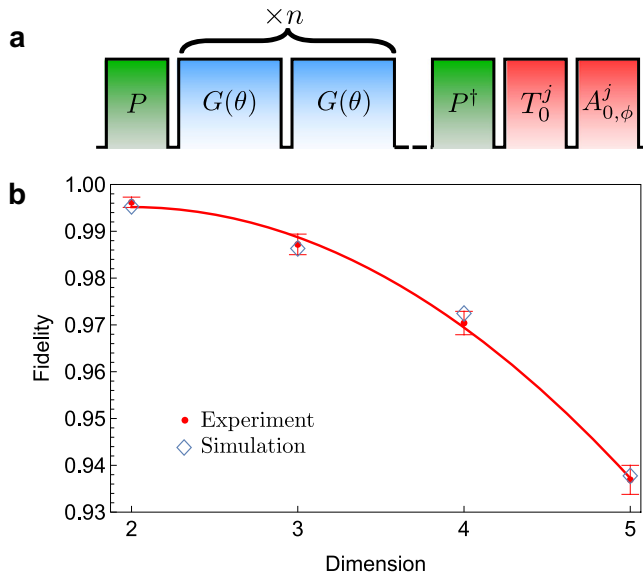


Fig. 4 | Fidelity decay measured using multiple gates. **a** Schematic of the measurement sequence. Two ions initialized in $|00\rangle$ are rotated into an equal superposition of all states by applying the operator P with the 729 nm laser. After applying the gate operator $G(\theta)$ a variable number of times n a reversed preparation pulse P^\dagger is applied. The populations of the resulting state are measured by a set of transfer pulses T_0^j , which are resonant π pulses between $|0\rangle \leftrightarrow |j\rangle$ to transfer the state $|j\rangle$ to the $S_{1/2}$ manifold, allowing us to distinguish the qudit states. An analysis pulse $A_{0,\phi}^j$ consisting of a resonant $\pi/2$ pulse between $|0\rangle \leftrightarrow |j\rangle$ with variable phase ϕ is used to measure the coherence between the $|0\rangle$ and $|j\rangle$ levels. Combined with the transfer pulses, all pairwise coherences can be measured. The average gate fidelities, shown as red circles, are extracted from fits to the fidelity decay when applying multiple gates $G(\theta)$ between P and P^\dagger . The error bars correspond to 1 standard deviation in the fit parameters. A quadratic curve has been fitted to the data to highlight the empirically observed scaling of the fidelity with dimension. The simulated fidelities from a detailed noise model are shown as blue diamonds, see supplementary note 2 for details.

photons on a photo-multiplier tube. Using additional π -pulses $T_0^j = R^{0j}(\pi, 0)$, the same procedure gives access to all components $|jj\rangle$. The coherence terms between the states $|00\rangle$ and $|jj\rangle$ are estimated by applying a $\pi/2$ -pulse $A_{0,\phi}^j = R^{0j}(\pi/2, \phi)$ with variable phase ϕ before performing the fluorescence readout. Applying T_0^k before $A_{0,\phi}^j$ allows us to measure the coherence between the states $|kk\rangle$ and $|jj\rangle$. We then extract the coherence between the two terms from the parity oscillations by Bayesian parameter estimation, which accounts for measurement statistics and guarantees that the results stay physically possible.

The observed fidelity is affected by state-preparation-and-measurement (SPAM) errors, including the pulses P , P^\dagger the transfer pulse T_0^j and analysis pulse $A_{0,\phi}^j$. In order to separate the errors from SPAM and gate $G(\theta)$ for each dimension d , we insert up to 9 applications of $G(\theta)$ between the pulses P and P^\dagger (see Fig. 4 (a)), and compute the state fidelity for each n that results in an entangled state. We then fit an exponential decay to estimate the fidelity of a single gate. Such repeated gate applications, however, are also sensitive to the presence of non-Markovian noise in our system that leads to deviations from purely exponential decay. The extracted fidelities should thus be interpreted as an estimate for the SPAM corrected average gate performance over a sequence of length n .

We apply this procedure for $d=2, 3, 4, 5$ and obtain fidelities of 99.6(1)%, 98.7(2)%, 97.0(3)%, 93.7(3)%, respectively. While the intrinsic limits on gate fidelity due to finite state lifetime and Raman beam scattering depend only weakly on the dimension d (see supplementary note 2), the measured gate performance degrades quadratically with

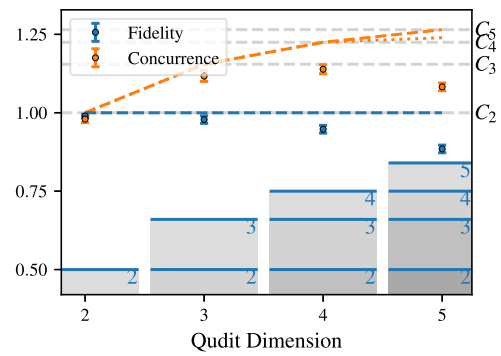


Fig. 5 | Generation of genuine qudit entanglement. The measured state fidelity for $d=2, 3, 4, 5$ is shown as blue data points and the corresponding concurrence as orange squares. The ideal values for maximally entangled states (the experimental target states) are shown as dashed (dotted) lines. The gray shaded bars represent the lower bound on the fidelity (blue data points) for certifying maximal Schmidt number entanglement, while the gray horizontal lines indicate the concurrence C_d for a maximally entangled state in dimension d . Error bars correspond to one standard deviation of experimental shot noise.

dimension as seen in Fig. 4 (b). This can be understood if the total gate error is dominated by technical noise sources that do not scale linearly with d . To investigate this we construct a numeric error model that computes the expected decay data using all independently measured error sources as inputs (see supplementary note 2), reproducing the observed data with very good agreement (blue diamonds in Fig. 4 (b)). This model suggests that while for $d=2$ the gate fidelity is limited by the motional coherence time of the ion and frequency noise of the gate laser, for higher dimension the dominant error sources become the gate Rabi frequency noise and slow frequency noise that causes dephasing of the local operations. We can hence conclude that the gate fidelity in higher dimensions can be significantly improved if technical noise sources such as magnetic field noise contributing to the aforementioned local operation dephasing or Rabi frequency fluctuations can be suppressed.

We furthermore evaluate the entanglement properties⁴¹ of the states generated by a single application of the gate, including the Schmidt number, Concurrence, and Entanglement of Formation, see Fig. 5 and supplementary note 3 for details. We find that the concurrence for all states with $d > 2$ significantly exceeds the maximal possible value for any qubit state. Crucially, while the concurrence growth is expected to slow asymptotically with dimension, the Schmidt number in each dimension is maximal, indicating the presence of genuine qudit entanglement up to $d=5$. The Schmidt number has also been suggested to play a crucial role in the computational complexity of a quantum system⁴².

Discussion

We have demonstrated an experimental realization of a gate that directly generates native qudit entanglement between two trapped ions. The major difference between previously demonstrated qudit entangling schemes¹⁷ and our scheme is that the gate natively couples to all transitions, whereby it creates entanglement between the multiple qudit levels in a single application of the gate rather than through repeated applications of qubit entangling operations that couple to individual transitions and thereby only generate two-level entanglement in each step. This fundamental difference dictates not only the kind of entangling dynamics that can be realized, but also the error contributions and requirements on the experimental control. As a result the calibration of our native qudit gate compares favorably to multiple applications of a pairwise entangling Mølmer-Sørensen gate. In the latter case, the gate requires careful adjustment of the entangling laser control parameters for each of the desired $|S\rangle \leftrightarrow |D\rangle$ transitions

including compensation for light shifts and induces undesired phase shifts on spectator levels, which have to be tracked. For our qudit phase gate, increasing the dimensionality of the entangling space just requires one extra local operation per additional $D_{5/2}$ sub-level to be calibrated and the power of the gate laser to be adjusted by a known analytical ratio that is not sensitive to qubit frequency shifts from light shifts or otherwise, since the gate beam is far off-resonant. Interestingly, while all demonstrated schemes for creating genuine qudit entanglement exhibit a linear increase in gate duration with qudit dimension, this may be overcome for some interactions at the cost of a linear increase in control parameters⁴³. Moreover, while we demonstrated a highly symmetrized version of the gate, exploiting different light shifts on different ground- and excited state levels allows for a wide range of gate actions, accessible through local operations alone.

Data availability

The data generated in this study is deposited on Zenodo at <https://doi.org/10.5281/zenodo.7688595>.

Code availability

The code used for simulation of the error budget is available upon request.

References

- Saffman, M. Quantum computing with neutral atoms. *Natl Sci. Rev.* **6**, 24 (2019).
- Huang, H.-L., Wu, D., Fan, D. & Zhu, X. Superconducting quantum computing: a review. *Sci. China Inform. Sci.* **63**, 180501 (2020).
- Bruzewicz, C. D., Chiaverini, J., McConnell, R. & Sage, J. M. Trapped-ion quantum computing: Progress and challenges. *Appl. Phys. Rev.* **6**, 021314 (2019).
- Slussarenko, S. & Pryde, G. J. Photonic quantum information processing: a concise review. *Appl. Phys. Rev.* **6**, 041303 (2019).
- Chi, Y. et al. A programmable qudit-based quantum processor. *Nat. Commun.* **13**, 1166 (2022).
- Ringbauer, M. et al. Certification and quantification of multilevel quantum coherence. *Phys. Rev. X* **8**, 041007 (2018).
- Wang, J. et al. Multidimensional quantum entanglement with large-scale integrated optics. *Science* **360**, 285 (2018).
- Ahn, J., Weinacht, T. & Bucksbaum, P. Information storage and retrieval through quantum phase. *Science* **287**, 463 (2000).
- Godfrin, C. et al. Operating quantum states in single magnetic molecules: implementation of Grover's quantum algorithm. *Phys. Rev. Lett.* **119**, 187702 (2017).
- Anderson, B. E., Sosa-Martinez, H., Riofrío, C. A., Deutsch, I. H. & Jessen, P. S. Accurate and robust unitary transformations of a high-dimensional quantum system. *Phys. Rev. Lett.* **114**, 240401 (2015).
- Gedik, Z. et al. Computational speed-up with a single qudit. *Sci. Rep.* **5**, 14671 (2015).
- Kononenko, M. et al. Characterization of control in a superconducting qutrit using randomized benchmarking. *Phys. Rev. Res.* **3**, L042007 (2021).
- Morvan, A. et al. Qutrit randomized benchmarking. *Phys. Rev. Lett.* **126**, 210504 (2021).
- Zhang, X. et al. State-independent experimental test of quantum contextuality with a single trapped ion. *Phys. Rev. Lett.* **110**, 070401 (2013).
- Hu, X.-M. et al. Beating the channel capacity limit for superdense coding with entangled ququarts. *Sci. Adv.* **4**, eaat9304 (2018).
- Blok, M. S. et al. Quantum information scrambling on a superconducting qutrit processor. *Phys. Rev. X* **11**, 021010 (2021).
- Ringbauer, M. et al. A universal qudit quantum processor with trapped ions. *Nat. Phys.* **18**, 1053 (2022).
- Senko, C. et al. Realization of a quantum integer-spin chain with controllable interactions. *Phys. Rev. X* **5**, 021026 (2015).
- Leupold, F. M. et al. Sustained state-independent quantum contextual correlations from a single ion. *Phys. Rev. Lett.* **120**, 180401 (2018).
- Malinowski, M. et al. Probing the limits of correlations in an indivisible quantum system. *Phys. Rev. A* **98**, 050102 (2018).
- Lanyon, B. P. et al. Simplifying quantum logic using higher-dimensional Hilbert spaces. *Nat. Phys.* **5**, 134 (2008).
- Wang, Y., Hu, Z., Sanders, B. C. & Kais, S. Qudits and high-dimensional quantum computing. *Front. Phys.* **8**, 479 (2020).
- Campbell, E. T., Anwar, H. & Browne, D. E. Magic-state distillation in all prime dimensions using quantum reed-muller codes. *Phys. Rev. X* **2**, 17 (2012).
- Duclos-Cianci, G. & Poulin, D. Kitaev's Z_d -code threshold estimates. *Phys. Rev. A* **87**, 062338 (2013).
- Anwar, H., Brown, B. J., Campbell, E. T. & Browne, D. E. Fast decoders for qudit topological codes. *New J. Phys.* **16**, 063038 (2014).
- Watson, F. H. E., Anwar, H. & Browne, D. E. Fast fault-tolerant decoder for qubit and qudit surface codes. *Phys. Rev. A* **92**, 032309 (2015).
- Stricker, R. et al. Experimental single-setting quantum state tomography. *PRX Quantum* **3**, 040310 (2022).
- Banuls, M. C. et al. Simulating lattice gauge theories within quantum technologies. *Eur. Phys. J. D* **74**, 165 (2020).
- González-Cuadra, D., Zache, T. V., Carrasco, J., Kraus, B. & Zoller, P. Hardware efficient quantum simulation of non-abelian gauge theories with qudits on rydberg platforms. *Phys. Rev. Lett.* **129**, 160501 (2022).
- Deller, Y. et al. Quantum approximate optimization algorithm for qudit systems with long-range interactions <https://doi.org/10.48550/ARXIV.2204.00340> (2022).
- MacDonell, R. J. et al. Analog quantum simulation of chemical dynamics. *Chem. Sci.* **12**, 9794 (2021).
- Kraft, T., Ritz, C., Brunner, N., Huber, M. & Gühne, O. Characterizing genuine multilevel entanglement. *Phys. Rev. Lett.* **120**, 060502 (2018).
- Brennen, G., Bullock, S. & O'Leary, D. Efficient circuits for exact-universal computation with qudits. *Quantum Information and Computation* **6**, 436 (2006).
- Leibfried, D. et al. Experimental demonstration of a robust, high-fidelity geometric two ion-qubit phase gate. *Nature* **422**, 412 (2003).
- Ballance, C. J., Harty, T. P., Linke, N. M., Sepiol, M. A. & Lucas, D. M. High-fidelity quantum logic gates using trapped-ion hyperfine qubits. *Phys. Rev. Lett.* **117**, 060504 (2016).
- Hughes, A. C. et al. Benchmarking a high-fidelity mixed-species entangling gate. *Phys. Rev. Lett.* **125**, 80504 (2020).
- Baldwin, C. H. et al. High-fidelity light-shift gate for clock-state qubits. *Phys. Rev. A* **103**, 012603 (2021).
- Sawyer, B. C. & Brown, K. R. Wavelength-insensitive, multispecies entangling gate for group-2 atomic ions. *Phys. Rev. A* **103**, 022427 (2021).
- Clark, C. R. et al. High-fidelity bell-state preparation with 40Ca^+ optical qubits. *Phys. Rev. Lett.* **127**, 130505 (2021).
- Brandl, M. F. et al. Cryogenic setup for trapped ion quantum computing. *Review of Scientific Instruments* **87**, 113103 (2016).
- Friis, N., Vitagliano, G., Malik, M. & Huber, M. Entanglement certification from theory to experiment. *Nat. Rev. Phys.* **1**, 72 (2019).
- Van den Nest, M. Universal quantum computation with little entanglement. *Phys. Rev. Lett.* **110**, 060504 (2013).
- Low, P. J., White, B. M., Cox, A. A., Day, M. L. & Senko, C. Practical trapped-ion protocols for universal qudit-based quantum computing. *Phys. Rev. Res.* **2**, 033128 (2020).

Acknowledgements

This project has received funding from the European Union's Horizon 2020 research and innovation program under the Marie

Skłodowska-Curie grant agreement No 840450. We gratefully acknowledge support by the EU Quantum Technology Flagship grant AQTION under Grant Agreement number 820495 and the EU Quantum Technology Flagship grant MILLENION, and by the US Army Research Office through Grant No. W911NF-21-1-0007. We also acknowledge funding by the European Research Council through the Consolidator grant ‘Cocoquest’ 101043705 and the Starting grant ‘QUDITS’ 101039522. Views and opinions expressed are however those of the author(s) only and do not necessarily reflect those of the European Union or the European Research Council. Neither the European Union nor the granting authority can be held responsible for them. We also acknowledge funding by the Austrian Science Fund (FWF), through the SFB BeyondC (FWF Project No. F7109), the START prize (Y879-N27), by the Austrian Research Promotion Agency (FFG) contract 872766, and by the IQI GmbH. The research is also based upon work supported by the Office of the Director of National Intelligence (ODNI), Intelligence Advanced Research Projects Activity (IARPA), via the US Army Research Office Grant No. W911NF-16-1-0070.

Author contributions

M.R. and P.H. conceived the project. P.H., B.W., L.G., and M.v.M. performed the experiments. P.H. and B.W. performed the numerical simulations. P.H., B.W., and L.G. analyzed the data. P.H., B.W., L.G., M.v.M., P.S., T.M., and M.R. contributed to the experimental setup and interpretation of the results. M.H. derived the theory results. R.B., P.S., T.M., and M.R. supervised the project. All authors contributed to writing the manuscript. P.H. and B.W. contributed equally to the work.

Competing interests

T.M. & R.B. are associated with Alpine Quantum Technologies, a commercially oriented quantum computing company. The remaining authors declare no other competing interests.

Additional information

Supplementary information The online version contains supplementary material available at <https://doi.org/10.1038/s41467-023-37375-2>.

Correspondence and requests for materials should be addressed to Pavel Hrmo.

Peer review information *Nature Communications* thanks the anonymous reviewer(s) for their contribution to the peer review of this work. Peer reviewer reports are available.

Reprints and permissions information is available at <http://www.nature.com/reprints>

Publisher’s note Springer Nature remains neutral with regard to jurisdictional claims in published maps and institutional affiliations.

Open Access This article is licensed under a Creative Commons Attribution 4.0 International License, which permits use, sharing, adaptation, distribution and reproduction in any medium or format, as long as you give appropriate credit to the original author(s) and the source, provide a link to the Creative Commons license, and indicate if changes were made. The images or other third party material in this article are included in the article’s Creative Commons license, unless indicated otherwise in a credit line to the material. If material is not included in the article’s Creative Commons license and your intended use is not permitted by statutory regulation or exceeds the permitted use, you will need to obtain permission directly from the copyright holder. To view a copy of this license, visit <http://creativecommons.org/licenses/by/4.0/>.

© The Author(s) 2023